



**HAL**  
open science

# Crystal-chemical and biological controls of trace and minor element incorporation into magnetite nanocrystals

Matthieu Amor, Damien Faivre, Daniel M. Chevrier

► **To cite this version:**

Matthieu Amor, Damien Faivre, Daniel M. Chevrier. Crystal-chemical and biological controls of trace and minor element incorporation into magnetite nanocrystals. 2022. hal-03841299

**HAL Id: hal-03841299**

**<https://hal.science/hal-03841299v1>**

Preprint submitted on 7 Nov 2022

**HAL** is a multi-disciplinary open access archive for the deposit and dissemination of scientific research documents, whether they are published or not. The documents may come from teaching and research institutions in France or abroad, or from public or private research centers.

L'archive ouverte pluridisciplinaire **HAL**, est destinée au dépôt et à la diffusion de documents scientifiques de niveau recherche, publiés ou non, émanant des établissements d'enseignement et de recherche français ou étrangers, des laboratoires publics ou privés.

1           **Crystal-chemical and biological controls of trace and**  
2           **minor element incorporation into magnetite nanocrystals**

3  
4                           *Matthieu Amor<sup>a\*</sup>, Damien Faivre<sup>a</sup>, Daniel M. Chevrier<sup>a\*</sup>*

5  
6                           *<sup>a</sup> Aix-Marseille Université, CEA, CNRS, BIAM, 13108 Saint-Paul-lez-Durance, France*

7  
8  
9           Keywords: Trace Element Partitioning, Magnetotactic Bacteria, Magnetite Nanoparticles,  
10           Biomineralization, Lattice and Crystal Field Theories

11  
12                           \*To whom correspondence should be addressed:  
13                           [matthieu.amor@cea.fr](mailto:matthieu.amor@cea.fr) (MA); [daniel.chevrier@cea.fr](mailto:daniel.chevrier@cea.fr) (DMC)

14  
15

## 16 **Abstract**

17 Magnetite nanoparticles possess numerous fundamental, biomedical and industrial applications,  
18 many of which depend on tuning the magnetic properties. This is often achieved by the  
19 incorporation of trace and minor elements into the magnetite lattice. Such incorporation was  
20 shown to depend strongly on the magnetite formation pathway (i.e., abiotic *vs* biological), but  
21 the mechanisms controlling element partitioning between magnetite and its surrounding  
22 precipitation solution remain to be elucidated. Here, we used a combination of theoretical  
23 modelling (lattice and crystal field theories) and experimental evidence (high-resolution  
24 inductively coupled plasma mass spectrometry and X-ray absorption spectroscopy) to  
25 demonstrate that element incorporation into abiotic magnetite nanoparticles is controlled  
26 principally by cation size and valence. Elements from the first series of transition metals (Cr to  
27 Zn) constituted exceptions to this finding as their incorporation appeared to be also controlled  
28 by the energy levels of their unfilled 3d orbitals, in line with crystal field mechanisms. We then  
29 show that element incorporation into biological magnetite nanoparticles produced by  
30 magnetotactic bacteria (MTB) cannot be explained by crystal-chemical parameters alone,  
31 which points to the biological control exerted by the bacteria over the element transfer between  
32 MTB growth medium and the intracellular environment. This screening effect generates  
33 biological magnetite with a purer chemical composition than the abiotic materials formed in a  
34 solution of similar composition. Our work establishes a theoretical framework for  
35 understanding the crystal-chemical and biological controls of trace and minor cation  
36 incorporation into magnetite, thereby providing predictive methods to tailor the composition of  
37 magnetite nanoparticles for improved control over magnetic properties.

## 38 **Main Text**

39 Magnetite [Fe(II)Fe(III)<sub>2</sub>O<sub>4</sub>] is a naturally-occurring ubiquitous Fe oxide that can be  
40 precipitated through abiotic chemical reactions<sup>1</sup>. Microorganisms can also promote magnetite  
41 formation. Among them, only magnetotactic bacteria (MTB) are known to synthesize  
42 nanoparticles of magnetite in a genetically controlled manner by incorporating Fe into  
43 organelles called magnetosomes for magnetite formation<sup>2</sup>. MTB are proposed to represent some  
44 of the most ancient microorganisms on Earth<sup>3</sup>, and are markers of oxic/anoxic transitions in the  
45 environment<sup>4</sup>. Nanoparticles of magnetite are of fundamental scientific interest in industrial  
46 and biomedical applications<sup>5,6,7</sup>, with many of these interests relying on careful tuning and  
47 optimization of magnetic properties. A particular way of doing so directly relies on modifying  
48 the chemical composition of magnetite, into which cations can substitute for Fe, incorporating  
49 into the magnetite lattice structure and thereby modifying its magnetic properties such as  
50 coercivity, saturation magnetization or heat release capacity<sup>8,9</sup>. Cation incorporation has been  
51 shown to depend strongly on the nature of the magnetite formation pathways (i.e., abiotic or  
52 biologic)<sup>10</sup>, but the mechanisms controlling such incorporation remain unknown.

53 The content of trace and minor elements in magnetite is also of critical interest for the  
54 detection of extra-terrestrial and ancient terrestrial life<sup>4</sup> as exemplified by the controversial  
55 origin of magnetite in the Martian meteorite ALH84001<sup>11</sup>. This meteorite contains nanocrystals  
56 of magnetite encapsulated in (Ca, Mg, Fe)-carbonates showing a pure chemical composition  
57 (i.e., they contain no detectable dopant elements)<sup>12</sup>. They were proposed to be produced from  
58 the thermal decomposition of the carbonate matrix<sup>13</sup>, although laboratory experimentation  
59 showed that incorporation of Mg and Ca into the generated magnetite should occur during such  
60 processes<sup>14</sup>. An alternative biological origin of this Martian magnetite was thus suggested, since  
61 only MTB were shown to generate magnetite with pure chemical composition<sup>10</sup>. Such unique  
62 property of biological magnetite was proposed as a reliable tool for the identification of fossils

63 of MTB in ancient terrestrial and extra-terrestrial environments<sup>4</sup>. Therefore, understanding the  
64 mechanisms leading to trace and minor element incorporation into magnetite, as well as the  
65 capacity of MTB to screen for element incorporation, has important implications in exobiology  
66 and (paleo)environmental sciences<sup>4</sup>.

67 In the present study, we establish the crystal-chemical parameters controlling the  
68 incorporation of trace and minor elements into magnetite nanocrystals. Using the  
69 concentrations of chemical elements measured from high-resolution inductively coupled  
70 plasma mass spectrometry (HR-ICP-MS)<sup>10</sup> in different series of abiotic magnetite, we show  
71 that the cation incorporation is controlled by the ionic radius and the valence. We do report a  
72 few exceptions: elements from the first series of transition metals (Cr, Mn, Co, Ni, Cu, Zn) are  
73 more stabilized into the magnetite lattice during precipitation than predicted from their size and  
74 valence. X-ray absorption microscopy (XAS) specifically on Mn, Co and Zn demonstrates  
75 demonstrate that the preferential incorporation of first series transition metals can be explained  
76 by the energy levels of unfilled 3d electron orbitals. Identifying this comprehensive framework  
77 of the crystal-chemical processes controlling element incorporation into magnetite enables us  
78 to investigate the biological control exerted by the magnetotactic strain *Magnetospirillum*  
79 *magneticum* AMB-1 on element partitioning between magnetite and the external solution<sup>10</sup>. We  
80 find that the behavior of elements during biological formation of magnetite cannot be explained  
81 by crystal-chemical parameters alone: their incorporation into MTB magnetite is more limited  
82 than expected given their ionic radius and valence. To establish the biological relevance of these  
83 findings, we prepared additional cultures of the magnetotactic *Magnetospirillum*  
84 *griphyswaldense* MSR-1, another model magnetotactic strain. HR-ICP-MS analyses of MSR-  
85 1 magnetite and residual growth medium complemented with trace elements yielded element  
86 partitioning similar to that observed in AMB-1, confirming a consistent application of  
87 biological control over metal incorporation. Furthermore, XAS analyses evidenced no

88 alteration of dopant cation size and valence in biological magnetite. These results point towards  
89 and active screening of elements by the bacteria to limit the transfer of trace and minor elements  
90 from the external solution to internally formed magnetite nanoparticles. Finally, we discuss the  
91 implications of our work for fundamental, environmental and biomedical applications of  
92 magnetite nanoparticles.

93

## 94 **Results and Discussion**

### 95 **Chemical composition of abiotic and biological magnetite**

96 Magnetite possesses an inverse spinel structure, with trivalent cations [Fe(III)] contained in  
97 both octahedral (6-coordination) and tetrahedral sites (4-coordination) while divalent cations  
98 [Fe(II)] occupy octahedral sites only<sup>1</sup>. During abiotic or biological formation, distinct trace and  
99 minor cations can substitute Fe(II) or Fe(III) by incorporating into the lattice structure. A  
100 previous study quantified the trace element content of abiotic and biological (AMB-1 strain)  
101 magnetite nanoparticles<sup>10</sup>. Magnetite nanoparticles were thoroughly purified in order to  
102 eliminate adsorbed elements. X-ray diffraction and high-resolution electron microscopy  
103 analyses of the samples revealed pure magnetite crystals, with no additional precipitated phases  
104 potentially induced by element doping<sup>10</sup>. The concentrations of trace and minor elements (X)  
105 in magnetite and in the residual solution after nanoparticle formation were measured using HR-  
106 ICP-MS. For each element, a partition coefficient ( $D^X$ ) between magnetite and solution was  
107 calculated from the equation:

108

$$109 \quad D^X = \frac{[X_{magnetite}]}{[X_{solution}]} \quad (1)$$

110

111 where  $[X_{magnetite}]$  and  $[X_{solution}]$  are the massic concentrations of an element X in magnetite and  
112 in the residual solution after precipitation, respectively, expressed in ppb. Thus, the partition

113 coefficient quantifies the capacity of an element to incorporate into magnetite and does not  
114 depend on the initial concentration of trace elements in the precipitation solution, at least in  
115 first approximation. We show below that element partitioning can be explained by crystal-  
116 chemical parameters according to established models, demonstrating that the element  
117 concentration used (100 ppb for each element) did not induce competition between elements  
118 for incorporation into magnetite. The same set of partition coefficients was calculated in the  
119 case of biological formation by AMB-1 with identical dopant concentrations in the initial  
120 study<sup>10</sup>. Elemental concentrations in the residual growth media as well as magnetite samples  
121 thoroughly purified were quantified using HR-ICP-MS. Measured elemental concentrations  
122 and partition coefficients are given in Tables S1 and S2.

123 We demonstrate below (see sections on the lattice strain theory and crystal field theory) that  
124 elements from the first series of transition metals (Cr, Mn, Co, Ni, Cu and Zn) behave in a  
125 distinct manner from other metal groups. To better understand the mechanisms leading to their  
126 incorporation during magnetite precipitation, we produced additional abiotic and biological  
127 (strain MSR-1) samples doped with a Mn/Co/Zn mixture. The redox state and coordination of  
128 Fe, Mn, Co, Zn in magnetite was determined using XAS. Analyses of Ni and Cu doping were  
129 also conducted, but the dopant metal concentration in biological magnetite samples was too low  
130 (Fig. S1), similar way to what has been reported for MSR-1<sup>15</sup>. Transmission electron  
131 microscopy and XAS characterization at the Fe K-edge of the magnetite samples are presented  
132 in Fig. 1. XAS spectra show that the produced material corresponds to magnetite via the close  
133 alignment of three near-edge features in addition to post-edge oscillations.

134

### 135 **Lattice strain control of element incorporation into magnetite**

136 The partitioning of a trace element between a given lattice site (M) and melts under high  
137 temperature and pressure conditions is controlled by the ion radius and valence<sup>16</sup>. For a given

138 valence ( $n+$ , with  $n = 1, 2, 3$  or  $4$ ), incorporation of a trace element is maximized when the ionic  
139 radius ( $r^X$ ) matches the size of the site  $M$  ( $r_{n+}^{0(M)}$ ). A shift from this ideal size generates an  
140 elastic deformation that is accommodated by the neighboring crystal lattice, translating into a  
141 penalty in energy for the ion incorporation and, consequently, into a decrease of  $D^X$ . A size  
142 shift of the same magnitude but with opposite sign corresponds to the same energy penalty. The  
143 distribution of  $D^X$  values for an isoivalent series of elements thus follows a parabolic trend with  
144 a maximum value ( $D_{n+}^{0(M)}$ ) corresponding to a fictive element perfectly matching the size of the  
145 lattice site (i.e., strain-compensated  $D^X$ )<sup>16</sup> (see Eqs. 2 and 3 in Materials and Methods).  
146 Similarly, heterovalent cation substitution entails accommodation of excess electric charge by  
147 the crystal lattice that will also translate into a penalty in energy for element incorporation<sup>16</sup>.  
148 Thus,  $D_{n+}^{0(M)}$  corresponding to each valence also follow a parabolic trend with a maximum  
149 coefficient  $D^{00(M)}$  corresponding to an ion causing no electrostatic charging (i.e., homovalent  
150 substitution).

151 We tested such a model in the case of magnetite to determine the role of ion radius and  
152 valence in the distribution of  $D^X$  but under different conditions at ambient temperature and  
153 atmospheric pressure. For all valences, the experimentally determined  $D^X$  plotted against their  
154 cation radius were close identical to the predicted values calculated from Eq. 2. This shows that  
155 the incorporation of most trace and minor elements into abiotic magnetite can be predicted by  
156 a lattice strain model. The strain-compensated  $D_{n+}^{0(M)}$  extracted from Fig. 2 and represented  
157 against ionic charge also followed the expected parabolic trend (Fig. 3) (Eq. 3 in Materials and  
158 Methods). The maximum  $D_{n+}^{0(M)}$  corresponding to  $D^{00(M)}$  was observed for a cation charge of  
159  $+2.7$ , almost identical to the bulk Fe valence in magnetite ( $+2.67$ ). Overall, the distribution of  
160  $D^X$  values determined experimentally in abiotic precipitation followed a lattice strain model,  
161 demonstrating that cation radius and valence control the incorporation of trace and minor

162 elements in abiotic magnetite. However, a few exceptions were observed: Cr(II), Cr(III), Mn(II),  
163 Co(II), Ni(II), Cu(II) and Zn(II) (grey circles in Fig. 2), which all belong to the first series of  
164 transition metals (3d metals) also containing Fe, showed higher  $D^X$  than expected from their  
165 radii and valence. Such preferential incorporation cannot be explained by potential co-  
166 precipitation of distinct (oxyhydr)oxides phases as shown by X-ray and diffraction and electron  
167 microscopy performed on the samples used for the determination of  $D^X$ <sup>10</sup>.

168 Next, we consider the partition coefficients of trace and minor elements between the  
169 biological magnetite and the growth medium, which shows a distinct picture from abiotic  
170 results (Fig. 2).  $D^X$  values were consistently lower than those predicted from a lattice strain  
171 model (Eq. 2). Such depletion corresponds to a factor of  $\sim 5 \times 10^1$  [Cs(I)] up to  $\sim 9 \times 10^7$  [La(III)].  
172 The range of variation for  $D^X$  was also narrower in the case of biological magnetite, with most  
173 values ranging between  $10^{-1}$  and  $10^2$ , compared to the  $D^X$  variation in abiotic magnetite of 7  
174 orders of magnitude (Rb to Bi). Finally, the distribution of partition coefficients could not be  
175 modeled by the lattice strain theory using Eq. 2, showing that crystal-chemical parameters  
176 cannot explain the partitioning of trace and minor elements between AMB-1 magnetite and the  
177 external growth medium.

178

### 179 **Crystal field constraints on element incorporation into magnetite and coordination of 3d** 180 **metals in magnetite**

181 Elements from the first series of transition metals, including Fe, possess unfilled 3d orbitals  
182 in at least one of their oxidation states<sup>17</sup>. The two sets of 3d orbitals, namely  $t_{2g}$  (i.e.,  $d_{xy}$ ,  $d_{xz}$ ,  
183  $d_{yz}$ ) and  $e_g$  (i.e.,  $d_{z^2}$  and  $d_{x^2-y^2}$ ), have different geometries with the electronegative charge  
184 pointing to distinct directions. In octahedral configuration, electrons from  $e_g$  orbitals directly  
185 face the negatively charged oxygen, which maximizes the electric repulsion and thus  
186 corresponds to more energetic configurations<sup>17</sup>. The opposite case is observed in tetrahedral

187 coordination. The origin and consequences of these electrostatic interactions on the energy  
188 levels of 3d orbitals is described by the crystal field theory<sup>17</sup>. For each element of a given  
189 valence, the crystal field stabilization energy (CFSE) was documented by McClure in  
190 octahedral and tetrahedral coordination<sup>18</sup>. The partitioning of Cr(II), Cr(III), Mn(II), Co(II),  
191 Ni(II), Cu(II) and Zn(II) during abiotic magnetite precipitation was modeled from their CFSE  
192 for both coordination configurations (Fig. S2). No clear correlation between  $\log D^X$  and CFSE  
193 values was observed, suggesting that coordination and/or valence of doping elements are not  
194 as expected. This needed to be confirmed to determine whether crystal field effects control the  
195 incorporation of 3d metals in magnetite.

196 We determined the coordination and valence of Mn, Co and Zn using XAS in both abiotic  
197 and biological magnetite. Abiotic syntheses and MSR-1 cultures were performed in the  
198 presence of Mn(II), Co(II) and Zn(II) under the same experimental mixed-doping conditions as  
199 described above for AMB-1. The  $D^X$  values corresponding to abiotic precipitation were almost  
200 identical to those previously obtained (see Tables S1 and S4), but  $D^X$  values obtained from  
201 MSR-1 were higher than those previously obtained with AMB-1 (Tables S2 and S4). Such  
202 discrepancy can be explained by the magnetite yield and intracellular Fe content in the two  
203 strains, where MSR-1 is known to incorporate more iron than AMB-1 under standard growth  
204 conditions used in the present contribution<sup>19</sup>. An increased mass of magnetite increases the total  
205 mass of trace elements contained in magnetite, which in turn decreases the concentrations of  
206 trace elements in the residual medium and lead to an increase of  $D^X$ . We thus calculated  
207 partition coefficients of Mn, Co and Zn normalized to Fe ( $D^{X/Fe}$ ) to compare values obtained  
208 from AMB-1 and MSR-1. They yielded similar results in both strains (Table S5).

209 Abiotic and biological magnetite samples were measured in powdered form at the respective  
210 dopant K-edges to confirm the site occupancy of doped metals in magnetite. Due to the dopant-  
211 level concentration of each metal in magnetite, fluorescence detection was employed to collect

212 XAS spectra. In the case of Co for abiotic magnetite nanoparticles, the fluorescence signal was  
213 too weak to collect usable spectra, which is understandable given the ten-fold lower Co  
214 concentration abiotic in magnetite relative to Mn and Zn (see Table S4). Nevertheless, from  
215 similar previous characterizations of Co-ferrite nanoparticles ( $\text{Co}_x\text{Fe}_{3-x}\text{O}_4$ ) prepared via  
216 different synthetic methods, Co is well known to occupy mainly octahedral sites<sup>20,21</sup>. K-edge  
217 XAS for Mn-doped abiotic magnetite shows an oxidation state between Mn(II) and Mn(III)  
218 when compared with Mn-based oxides (Fig. 4A). This is reflected by the position of both the  
219 pre-edge position and the main rising edge (Fig. 4A, inset). Near-edge features of Mn-doped  
220 magnetite correspond more so with a Mn-ferrite reference ( $\text{Mn}_{0.5}\text{Fe}_{2.5}\text{O}_4$ )<sup>22</sup> indicating similar  
221 chemical and structural environment. However, weaker pre-edge and post-edge features (6562  
222 eV) potentially originate from the dilute and inhomogeneous nature of the dopant metal in the  
223 magnetite lattice compared to the Mn-ferrite reference. The difference in relative peak  
224 intensities when compared to the reference material may also indicate a partial change in  
225 octahedral/tetrahedral site occupancy. Although the extended X-ray absorption fine structure  
226 (EXAFS) region is too weak to fit scattering paths for structural information, *ab initio*  
227 simulations of the Mn K-edge X-ray absorption near-edge structure (XANES) for tetrahedral  
228 and octahedral Mn substitutions in magnetite (Fig. S3) confirm near-edge absorption features  
229 from both  $\text{Mn}_{0.5}\text{Fe}_{2.5}\text{O}_4$  reference and Mn-doped abiotic magnetite match with tetrahedral  
230 coordination. Zinc K-edge XAS for Zn-doped abiotic magnetite (Fig. 4C) has poorly defined  
231 near-edge features and very weak EXAFS. When compared with a Zn-ferrite reference  
232 ( $\text{ZnFe}_2\text{O}_4$ ), known to have a normal spinel crystal structure with Zn(II) occupying tetrahedral  
233 sites, the width and positioning of the XANES aligns well but the specific near-edge features  
234 are less apparent. Linear combination fitting with Zn-based references revealed a contribution  
235 of  $\text{ZnFe}_2\text{O}_4$  (41%) and octahedral Zn(II) complexes (59%) (Fig. S4). We attribute octahedral

236 Zn(II) complexes to be Zn sites allocated on the nanoparticle surface with short-range order or  
237 Zn(II) complexes adhered to the nanoparticle surface.

238 Higher quality data was obtained for biological magnetite, since dopants were found to be  
239 in higher concentration than in the abiotic samples, at least partially due to the high initial  
240 concentrations used in the bacterial growth media (Table S4). Cobalt K-edge XAS for Co-  
241 doped biological magnetite highly resembles that of a Co-ferrite reference ( $\text{CoFe}_2\text{O}_4$ ) (Fig. 4B),  
242 given the identical energies of distinctive near-edge features. From known crystal structure of  
243 Co-ferrite nanoparticles<sup>23,24</sup>, Co mainly occupies octahedral sites in magnetite in line with  
244 previous work on MTB<sup>25,26</sup>. Manganese K-edge XANES of Mn-doped biological magnetite is  
245 again similar to the  $\text{Mn}_{0.5}\text{Fe}_{2.5}\text{O}_4$  reference (Fig. 4A), with peak positions and their relative  
246 intensities even more comparable. The higher data quality for this sample afforded  
247 supplemental EXAFS information and a well-resolved pre-edge region. Regarding the latter  
248 (Fig. 4A, inset) and remarking on simulations performed (Fig. S3), a second pre-edge feature  
249 is observable for Mn-doped biological magnetite (Fig. S3, see features i and ii) that can be  
250 attributed as a partial +3 valence state of the dopant<sup>27</sup>. EXAFS fitting yielded a Mn-O  
251 coordination number of 3.7 and a bond distance of 202 pm (Fig. S5 and Table S6), both  
252 suggesting a tetrahedral environment for Mn dopants is likely, consistent with another recent  
253 study<sup>15</sup>. Nevertheless, a small contribution of Mn-Fe single scattering from Mn in octahedral  
254 sites (coordination number 1.9, bond distance 299 pm) was found to complete EXAFS fitting  
255 of Mn-O and Mn-Fe (coordination number 13.1, bond distance 352 pm) scattering from Mn in  
256 tetrahedral sites.

257 Zn XANES features are more prominent for Zn-doped biological magnetite than for the  
258 abiotic case, with near-edge features more resembling the Zn-ferrite reference material (Fig.  
259 4C). From linear combination fitting, we obtain 78%  $\text{ZnFe}_2\text{O}_4$  and 22% octahedral Zn(II)  
260 complexes for the Zn-doped biological magnetite (Fig. S4), indicating a higher contribution of

261 Zn incorporated into magnetite with tetrahedral coordination. EXAFS fitting of Zn-O path  
262 yielded a coordination number of 3.9 and bond distance of 205 pm confirming Zn mainly  
263 occupy tetrahedral sites. In our case, we note a high incorporation of Zn into MSR-1 magnetite  
264 as normal spinel  $ZnFe_2O_4$  from doping bacteria growth media with Zn(II), whereas another  
265 study found more ZnO than  $ZnFe_2O_4$ <sup>15</sup>.

266 Using the experimentally determined coordination and valence of Mn, Co and Zn, a  
267 corrected CFSE was calculated. As mentioned above, Mn in abiotic magnetite showed mixed  
268 +2/+3 valence. The rising edge position (determined from the first derivative maximum of the  
269 main absorption edge) was shifted towards higher values when compared to the Mn-ferrite  
270 reference. This indicates more oxidized Mn in the abiotic magnetite samples than in the ferrite  
271 reference, which has been shown to contained 25% Mn(III) and 75% Mn(II)<sup>28</sup>, while the  
272 biological magnetite overlapped the Mn-ferrite reference which suggests a similar valence for  
273 Mn. Therefore, the Mn(III) / total Mn ratios in the abiotic and biologic magnetite were taken as  
274 0.3 (i.e., higher than Mn-ferrite reference) and 0.25 (i.e., similar to Mn-ferrite reference),  
275 respectively. Zinc coordination was considered to be 60% octahedral / 40% tetrahedral in the  
276 abiotic magnetite, and 20% octahedral / 80% tetrahedral in the biological nanoparticles based  
277 on the fitting results. Finally, Co was considered to mainly occupy octahedral sites based on  
278 the extensive literature<sup>29,30</sup> that is consistent with present Co-doped MSR-1 magnetite.  
279 Measured partition coefficients represented against XAS-corrected CFSE are shown in Fig. 5.  
280 In the abiotic case,  $\log D^X$  values showed a weak linear relationship with CFSE (correlation  
281 coefficient of 0.87), while biological  $\log D^X$  showed almost constant values with no correlation  
282 with CFSE (correlation coefficient of 0.006) (Fig. 5A). To take into account crystal field  
283 controls independently of lattice strain mechanisms, the measured partition coefficients in  
284 abiotic nanoparticles were normalized to the  $D^X$  predicted from lattice strain theory (Eq. 2 and  
285 Fig. 2). The results are presented in Fig. 5B and show a stronger linear correlation between the

286 trace element stabilization and the corrected CFSE (correlation coefficient of 0.99). Our results  
287 thus demonstrate the importance of taking into account the actual coordination of trace 3d  
288 metals in magnetite since their incorporation is controlled by crystal field mechanisms.

289

### 290 **Biological control over element transfer to magnetosomes in magnetotactic bacteria**

291 Our work aimed at understanding the mechanisms controlling the incorporation of cations  
292 distinct from Fe into magnetite. It demonstrates that partitioning of trace and minor elements  
293 between abiotic magnetite and surrounding solution is controlled by cation radius and valence,  
294 as well as the energy levels of 3d orbitals for elements from the first series of transition metals  
295 (Cr to Zn). The biological case showed a distinct picture as the distribution of  $D^X$  could not be  
296 modeled from lattice strain and crystal field theories alone. The low partition coefficients and  
297 low variation of  $D^X$  in the biological conditions are in line with the proposed hypothesis of Fe  
298 biopurification during magnetite formation, establishing the chemical purity of magnetite as a  
299 signature of MTB activity.

300 The variability induced by MTB on trace and minor element partitioning could arise from  
301 the homeostasis of chemical conditions (pH, redox potential, etc.) in the intracellular  
302 environment, which are distinct from the external solution and maintained by the metabolic  
303 activity of the bacteria. They control the cation valence and speciation (and thus its size) in  
304 solution, which may in turn shift element partitioning (Eqs 2 and 3, Figs. 2 and 3). As evidenced  
305 by XAS measurements (linear fitting and comparison to references), the biological control over  
306 magnetite nanoparticle formation enables more homogeneous incorporation of dopants into the  
307 crystal lattice compared to the abiotic nanoparticles also produced under ambient conditions.  
308 We hypothesize that such homogeneous incorporation of dopant elements in biological  
309 magnetite could be due to the slow formation of magnetite in MTB (3 days of growth) compared  
310 to the abiotic nanoparticles which precipitates as soon as the pH conditions are favorable (see

311 materials and methods). However, the variability of cation size and valence evidenced by XAS  
312 measurements is too low to account for the decrease of  $D^X$  in the biological conditions (up to  
313 7 orders of magnitude, see Fig. 2)

314 Although not demonstrated, the lower levels of doped cations in biological magnetite were  
315 discussed as being caused by active and selective Fe incorporation into magnetosomes that  
316 excludes distinct elements<sup>10</sup>. Magnetite in MTB precipitates from a medium contained in lipid  
317 vesicles that is physically separated from the external solution and isolated from doping  
318 elements (i.e., the bacterial growth medium), diminishing their level of incorporation. A notable  
319 difference between both conditions of magnetite precipitation is the remarkable decrease of  
320 partition coefficients in bacterial cultures as all elements showed lower  $D^X$  values than those  
321 predicted from the lattice strain theory (Fig. 2). As detailed in the above section, an increased  
322 Fe precipitation into abiotic magnetite (i.e., a higher  $D^{Fe}$  partition coefficient) compared to  
323 biological conditions would lead to an increase of  $D^X$ . However, the decrease of  $D^{Fe}$  in the  
324 biological conditions when compared to abiotic syntheses is too limited to account for the low  
325  $D^X$  in AMB-1 and MSR-1 cultures (Fig. 2 and Table S4). This was also demonstrated in  
326 previous work discussing the distribution of partition coefficients normalized to Fe<sup>10</sup>.

327 The range of partition coefficients was also narrower in AMB-1 cultures compared to abiotic  
328 magnetite (Figs. 2 and 6). Consequently, the enrichment of trace elements in AMB-1 magnetite  
329 quantified by the ratio of measured  $D^X$  normalized to  $D^X$  values predicted from the lattice  
330 strain theory decreases linearly with the increase of cation radius, up to the ideal size ( $r_{n+}^{0(M)}$ )  
331 that is associated with the maximum  $D^X$  (Fig. 6). Enrichment of doping elements in MTB  
332 magnetite then increases again for cation radii higher than  $r_{n+}^{0(M)}$  (Figs. 6A and 6D).  
333 Accordingly, the depletion of trace and minor elements from MTB magnetite is higher for  
334 elements showing high affinity for magnetite, and minimal for cations with the lowest abiotic  
335  $D^X$  (Fig. 6). This illustrates a screening effect induced by the bacterial membranes that limits

336 the transfer of cations distinct from Fe from the external solution to the location of magnetite  
337 formation regardless of the cation size and valence. Two exceptions are observed. Silver was  
338 more enriched in AMB-1 magnetite than the rest of the monovalent elements (Fig. 6A). This  
339 could reflect the antimicrobial properties of Ag(I)<sup>31</sup> and its sequestration into magnetite for  
340 detoxification as previously proposed for toxic cations<sup>32</sup>. Alternatively, such preferential  
341 inclusion of Ag in AMB-1 could arise from passive diffusion between the external solution and  
342 the intracellular medium. Additionally, Sr was more excluded from AMB-1 magnetite than  
343 other divalent elements (Fig. 6). Exposure to Sr was shown to induce efflux systems in  
344 bacteria<sup>33</sup>, and Sr is known to disturb Ca metabolism in animals<sup>34</sup>. Low  $D^{Sr}$  might thus be  
345 generated by Sr pumping outside of the cell to maintain homeostasis.

346

## 347 **Conclusion**

348 The present contribution establishes an experimental and theoretical framework that can  
349 predict the behavior of trace and minor cations during synthetic magnetite formation based on  
350 their size, valence and unfilled 3d orbitals. This enabled us to elucidate the screening effect  
351 MTB have on biological magnetite formation. Beyond the geobiological interests for the  
352 identification of ancient terrestrial and extra-terrestrial life, our work has significant  
353 implications for nanotechnological applications of biological and/or abiotic nanoparticles of  
354 magnetite. Deliberate doping of trace and minor elements has been carried out to optimize  
355 magnetite nanoparticle composition for dedicated applications, including doping of Co and Zn  
356 that increase the efficiency of magnetite's magnetic properties for cancer treatment using  
357 hyperthermia<sup>8,9,35</sup>, as well as its capacity of organic pollutant remediation and (bio)remediation  
358 of contaminated water<sup>36-38</sup>. The appropriateness of doped magnetite nanomaterials with tailored  
359 properties (e.g., magnetism) for future applications can be evaluated with our methodology by  
360 identifying the different outcomes of dopant composition via abiotic or biological synthesis.

361

## 362 **Materials and Methods**

### 363 **Magnetite abiotic synthesis**

364 Production of abiotic magnetite nanoparticles was performed using a titration device as  
365 already described<sup>39</sup>. An Fe chloride mixture ( $[\text{Fe(II)Cl}_2] = 0.33 \text{ M}$  and  $[\text{Fe(III)Cl}_3] = 0.66 \text{ M}$ )  
366 was added to a NaOH solution ( $\text{pH} = 11$ ) at room-temperature. The decrease of pH associated  
367 with the release of protons during magnetite precipitation was compensated by adding  
368 additional NaOH solution (1 M) to keep the pH constant throughout the experiment. The doping  
369 elements were added at similar concentrations (100 ppb for each element) in the Fe mixture.  
370 The Fe mixture, NaOH solution, and the magnetite precipitation solution were kept under  
371 constant anoxic conditions by flushing  $\text{N}_2$  to prevent Fe(II) oxidation. Magnetite samples were  
372 then recovered by centrifugation (8 000 rpm for 15 min), rinsed two times with Milli-Q water  
373 and dried in a desiccator. All samples were kept under anoxic conditions before XAS analyses.

374

### 375 **Bacterial cultures and magnetite purification**

376 The MSR-1 strain was cultivated under standard conditions following a previously  
377 published protocol<sup>19</sup>. Because MTB magnetite is strongly depleted in dopant elements  
378 compared to its abiotic counterpart<sup>10</sup>, Mn, Co and Zn were added at higher concentration to  
379 maximize their incorporation into MSR-1 magnetite for XAS measurements. Doping elements  
380 were added at similar concentrations (33  $\mu\text{M}$  for each element in the mixed-element condition,  
381 and 100  $\mu\text{M}$  for single-doped samples) in MSR-1 growth medium. MSR-1 magnetite was then  
382 extracted for XAS and HR-ICP-MS analyses: MSR-1 bacteria were lysed using a French Press  
383 (3 runs at 7 000 kPa), recovered with a magnet, and purified with an EDTA-Triton-SDS  
384 preparation following a previously described procedure<sup>10</sup>.

385

386 **Transmission electron microscopy**

387 Abiotic magnetite nanoparticles and MSR-1 bacteria were deposited on carbon-coated  
388 copper grids for electron microscopy characterizations. MSR-1 grids were rinsed using Milli-  
389 Q water to remove salts precipitated from the growth medium. Samples were then observed  
390 with a FEI Tecnai G2 Biotwin microscope operating at 100 kV.

391

392 **Selection of trace and minor elements**

393 Four elements (B, Ca, K, Mg) from the initial work<sup>10</sup> were excluded for the present work: B  
394 and K are contained in the glassware (borosilicates) used for the preparation and storage of  
395 samples, and thus contaminate the magnetite and solution samples, while only one replicate  
396 could be obtained in the case of Ca and Mg.

397

398 **Determination of element oxidation state in solution and magnetite**

399 The oxidation state of all doping trace and minor elements in precipitation solutions was  
400 determined at the pH /  $E_h$  conditions representative of the abiotic precipitation solution and the  
401 proposed magnetosome internal solution<sup>40</sup> with the geochemical code CHESS<sup>41</sup> using the  
402 THERMOTDEM<sup>42</sup> database. Because Fe(II) is found in octahedral sites in magnetite, all  
403 divalent cations were considered as occupying octahedral sites in magnetite. Similarly, half of  
404 Fe(III) is present in octahedral sites magnetite, the other half being contained in tetrahedral sites.  
405 We thus considered trivalent cations to be incorporated in both 6- (50%) and 4-coordination  
406 (50%).

407

408 **Prediction of trace and minor element partition coefficients from lattice strain theory**

409 The distribution of  $D^X$  values for an isovalent series of elements can be described by<sup>16</sup>:

410

411 
$$D^X = D_{n+}^{0(M)} \times \exp \left\{ \frac{-4\pi N_A E_{n+}^M \left[ \frac{1}{2} r_{n+}^{0(M)} (r^X - r_{n+}^{0(M)})^2 + \frac{1}{3} (r^X - r_{n+}^{0(M)})^3 \right]}{RT} \right\} \quad (2)$$

412

413 With  $D_{n+}^{0(M)}$  the partition coefficient for a fictive element with  $r^X = r_{n+}^{0(M)}$  and causing no  
 414 elastic strain (i.e. strain-compensated  $D^X$ ),  $E_{n+}^M$  the lattice strain parameter describing the  
 415 Young's Modulus (in GPa) of the site M,  $N_A$  the Avogadro's number, R the perfect gas constant,  
 416 and T the temperature in Kelvin. Similarly, heterovalent cation substitution entail excess  
 417 electric charge accommodated by the crystal lattice that will also translate into a penalty in  
 418 energy for element incorporation<sup>16</sup>:

419

420 
$$D_{n+}^{0(M)} = D^{00(M)} \times \exp \left\{ \frac{-N_A e^2 (Z^X - Z^{0(M)})^2}{(2\varepsilon\rho RT)} \right\} \quad (3)$$

421

422 Where  $D^{00(M)}$  is the strain-compensated partition coefficient for a fictive ion causing no  
 423 electrostatic charging (i.e. homovalent substitution), e the electron charge,  $\rho$  the radius of the  
 424 region over which the excess charge is distributed,  $\varepsilon$  the dielectric constant of that region, and  
 425  $Z^X$  and  $Z^{0(M)}$  the ionic charge and the optimum ionic charge at the site M, respectively.

426 The parameters used for the calculation of predicted partition coefficients using Eq. 2 ( $D_{n+}^{0(M)}$ ,  
 427  $r_{n+}^{0(M)}$ , and  $E_{n+}^M$ ) are given in Table S3. Selected Young's modulus range between 85 and 470  
 428 GPa, which is in good agreement with the range of published values for macrocrystals and  
 429 nanoparticles of magnetite<sup>43-45</sup>. Higher variability in  $E_{n+}^M$  than that observed here for magnetite  
 430 has already been reported in many mineral phases, including plagioclase, diopside, augite,  
 431 anorthite, albite, diopside or fluorite<sup>46,47</sup>. Such variability is related to the ion charge and the  
 432 cation – oxygen distance<sup>16</sup>. In the case of magnetite, it can also be explained by the variability  
 433 induced by the two lattice sites under consideration (tetrahedral and octahedral). For Eq. 3, a

434 dielectric constant ( $\epsilon$ ) of 50 and a lattice region with a radius ( $\rho$ ) of 17 nm were considered (Fig.  
435 3). Such values correspond to published  $\epsilon$  for magnetite<sup>48,49</sup> and to the size of the magnetite  
436 nanoparticles produced for the determination of their trace element composition, respectively.

437

### 438 **Inductively Coupled Plasma – Mass Spectrometry (ICP-MS) analyses**

439 The concentrations of Fe, Mn, Co and Zn in the abiotic and MSR-1 magnetite nanoparticles,  
440 in the residual precipitation solution and in the residual bacterial growth media were determined  
441 using a Perkin Elmer NexIon 300X mass spectrometer (collision mode configuration with a  
442 Rh103 internal standard) at the *Centre Européen de Recherche et d'Enseignement en*  
443 *Géosciences de l'Environnement* (CEREGE Aix-en-Provence, France). Three replicates were  
444 performed for each experimental conditions.

445

### 446 **X-ray Absorption Spectroscopy (XAS)**

447 The abiotic and biological magnetite samples were measured under cryogenic conditions in  
448 powdered form. To prepare the samples for measurement, the purified abiotic and biological  
449 magnetite nanoparticles were spread onto Kapton tape and folded to seal the sample. The  
450 samples were kept frozen during storage, shipment and measurement. Principal data was  
451 collected at the I20-Scanning beamline (Diamond Light Source, Didcot, UK). Preliminary XAS  
452 data (additional Fe, Ni and Cu K-edge spectra) was collected at the Sector BM-20 beamline  
453 (Advanced Photon Source, Argonne National Laboratory, IL, USA). Due to the dilute nature  
454 of dopant metals, fluorescence detection was employed to collect XAS spectra. Several scans  
455 were collected and averaged to produce the spectra presented in this work. We note that Zn  
456 metal contamination (I20-Scanning data) was discovered after data collection and was  
457 attributed to a custom-printed sample holder used at the beamline. Linear combination fitting  
458 with a Zn metal reference accounts for this contribution. XAS data from Zn(II)-citrate and

459 Zn(II)-histadine complexes were implemented to fit as octahedral Zn(II) complexes. XAS of  
460 reference foils for Mn, Co and Zn were simultaneously collected downstream via ionization  
461 chambers for energy calibration. Athena and WinXAS programs were used for background  
462 subtraction, energy calibration, normalization and transformation to FT-EXAFS spectra.  
463 Athena was implemented for linear combination fitting and WinXAS for refined EXAFS fitting.  
464 The computational package FEFF8.2 was employed to simulate scattering paths for EXAFS  
465 fitting and to simulate Mn K-edge XANES of Mn in octahedral and tetrahedral lattice sites in  
466 magnetite.

467

## 468 **Acknowledgements**

469 MA is supported by a grant through the *Fondation pour la Recherche Médicale*  
470 (ARF201909009123). DMC acknowledges research funding through a European Union Marie-  
471 Skłodowska Curie Action International Fellowship (MSCA-IF Project 797431:  
472 BioNanoMagnets) and from a CNRS starting grant. CLS@APS facilities (Sector 20-BM) at the  
473 Advanced Photon Source (APS) are supported by the U.S. Department of Energy (DOE),  
474 NSERC Canada, the University of Washington, the Canadian Light Source (CLS), and the APS.  
475 Use of the APS is supported by the DOE under Contract No. DE-AC02-06CH11357. We  
476 acknowledge Diamond Light Source for beamtime on I20-Scanning under proposal SP25495.  
477 We thank the beamline scientists Michael Pape (APS) and Fred Mosselmans (DLS) for their  
478 technical assistance during beamtimes. The groups of Thomas N. Stokes, Alicia Muela and M.  
479 Luisa Fdez-Gubieda are thanked for sharing XAS data on ferrite references. Fred Mosselmans  
480 is also thanked for sharing Zn-based references. We thank Bernard Angeletti and Jean-Paul  
481 Ambrosi from the *Centre Européen de Recherche et d'Enseignement des Géosciences de*  
482 *l'Environnement* (Aix-en-Provence, France) for assistance with the mass spectrometry

483 measurements. We thank Paul N. Duchesne for constructive feedback and comments on the  
484 manuscript.

- 486 (1) Usman, M.; Byrne, J. M.; Chaudhary, A.; Orsetti, S.; Hanna, K.; Ruby, C.; Kappler,  
487 A.; Haderlein, S. B. Magnetite and Green Rust: Synthesis, Properties, and Environmental  
488 Applications of Mixed-Valent Iron Minerals. *Chem. Rev.* **2018**, *118* (7), 3251–3304.  
489 <https://doi.org/10.1021/acs.chemrev.7b00224>.
- 490 (2) Uebe, R.; Schueler, D. Magnetosome Biogenesis in Magnetotactic Bacteria. *Nat. Rev.*  
491 *Microbiol.* **2016**, *14* (10), 621–637. <https://doi.org/10.1038/nrmicro.2016.99>.
- 492 (3) Lin, W.; Paterson, G. A.; Zhu, Q.; Wang, Y.; Kopylova, E.; Li, Y.; Knight, R.;  
493 Bazylinski, D. A.; Zhu, R.; Kirschvink, J. L.; Pan, Y. Origin of Microbial Biomineralization  
494 and Magnetotaxis during the Archean. *Proc. Natl. Acad. Sci. U. S. A.* **2017**, *114* (9), 2171–  
495 2176. <https://doi.org/10.1073/pnas.1614654114>.
- 496 (4) Amor, M.; Mathon, F. P.; Monteil, C. L.; Busigny, V.; Lefevre, C. T. Iron-  
497 Biomineralizing Organelle in Magnetotactic Bacteria: Function, Synthesis and Preservation in  
498 Ancient Rock Samples. *Environ. Microbiol.* **2020**, *22* (9), 3611–3632.  
499 <https://doi.org/10.1111/1462-2920.15098>.
- 500 (5) Plan Sangnier, A.; Preveral, S.; Curcio, A.; K A Silva, A.; Lefèvre, C. T.; Pignol, D.;  
501 Lalatonne, Y.; Wilhelm, C. Targeted Thermal Therapy with Genetically Engineered  
502 Magnetite Magnetosomes@RGD: Photothermia Is Far More Efficient than Magnetic  
503 Hyperthermia. *J Control Release* **2018**, *279*, 271–281.  
504 <https://doi.org/10.1016/j.jconrel.2018.04.036>.
- 505 (6) Felfoul, O.; Mohammadi, M.; Taherkhani, S.; de Lanauze, D.; Xu, Y. Z.; Loghin, D.;  
506 Essa, S.; Jancik, S.; Houle, D.; Lafleur, M.; Gaboury, L.; Tabrizian, M.; Kaou, N.; Atkin, M.;  
507 Vuong, T.; Batist, G.; Beauchemin, N.; Radzioch, D.; Martel, S. Magneto-Aerotactic Bacteria  
508 Deliver Drug-Containing Nanoliposomes to Tumour Hypoxic Regions. *Nat. Nanotechnol.*  
509 **2016**, *11* (11), 941–947. <https://doi.org/10.1038/NNANO.2016.137>.
- 510 (7) Zingsem, B. W.; Feggeler, T.; Terwey, A.; Ghaisari, S.; Spoddig, D.; Faivre, D.;  
511 Meckenstock, R.; Farle, M.; Winklhofer, M. Biologically Encoded Magnonics. *Nature*  
512 *Communications* **2019**, *10* (1), 4345. <https://doi.org/10.1038/s41467-019-12219-0>.
- 513 (8) Byrne, J. M.; Coker, V. S.; Moise, S.; Wincott, P. L.; Vaughan, D. J.; Tuna, F.;  
514 Arenholz, E.; van der Laan, G.; Patrick, R. a. D.; Lloyd, J. R.; Telling, N. D. Controlled  
515 Cobalt Doping in Biogenic Magnetite Nanoparticles. *Journal of The Royal Society Interface*  
516 **2013**, *10* (83), 20130134. <https://doi.org/10.1098/rsif.2013.0134>.
- 517 (9) Byrne, J. M.; Coker, V. S.; Cespedes, E.; Wincott, P. L.; Vaughan, D. J.; Patrick, R.  
518 A. D.; Laan, G. van der; Arenholz, E.; Tuna, F.; Bencsik, M.; Lloyd, J. R.; Telling, N. D.  
519 Biosynthesis of Zinc Substituted Magnetite Nanoparticles with Enhanced Magnetic  
520 Properties. *Advanced Functional Materials* **2014**, *24* (17), 2518–2529.  
521 <https://doi.org/10.1002/adfm.201303230>.
- 522 (10) Amor, M.; Busigny, V.; Durand-Dubief, M.; Tharaud, M.; Ona-Nguema, G.; Gélabert,  
523 A.; AlphanDéry, E.; Menguy, N.; Benedetti, M. F.; Chebbi, I.; Guyot, F. Chemical Signature  
524 of Magnetotactic Bacteria. *Proc. Natl. Acad. Sci. U. S. A.* **2015**, *112* (6), 1699–1703.  
525 <https://doi.org/10.1073/pnas.1414112112>.
- 526 (11) Thomas-Keprta, K. L.; Bazylinski, D. A.; Kirschvink, J. L.; Clemett, S. J.; McKay, D.  
527 S.; Wentworth, S. J.; Vali, H.; Gibson, E. K.; Romanek, C. S. Elongated Prismatic Magnetite  
528 Crystals in ALH84001 Carbonate Globules: Potential Martian Magnetofossils. *Geochim.*  
529 *Cosmochim. Acta* **2000**, *64* (23), 4049–4081. [https://doi.org/10.1016/S0016-7037\(00\)00481-](https://doi.org/10.1016/S0016-7037(00)00481-6)  
530 [6](https://doi.org/10.1016/S0016-7037(00)00481-6).
- 531 (12) Thomas-Keprta, K. L.; Clemett, S. J.; McKay, D. S.; Gibson, E. K.; Wentworth, S. J.  
532 Origins of Magnetite Nanocrystals in Martian Meteorite ALH84001. *Geochim. Cosmochim.*  
533 *Acta* **2009**, *73* (21), 6631–6677. <https://doi.org/10.1016/j.gca.2009.05.064>.

- 534 (13) Golden, D. C.; Ming, D. W.; Schwandt, C. S.; Lauer, H. V.; Socki, R. A.; Morris, R.  
535 V.; Lofgren, G. E.; McKay, G. A. A Simple Inorganic Process for Formation of Carbonates,  
536 Magnetite, and Sulfides in Martian Meteorite ALH84001. *Am. Miner.* **2001**, *86* (3), 370–375.
- 537 (14) Jimenez-Lopez, C.; Rodriguez-Navarro, C.; Rodriguez-Navarro, A.; Perez-Gonzalez,  
538 T.; Bazylnski, D. A.; Lauer, H. V.; Romanek, C. S. Signatures in Magnetites Formed by  
539 (Ca,Mg,Fe)CO<sub>3</sub> Thermal Decomposition: Terrestrial and Extraterrestrial Implications.  
540 *Geochim. Cosmochim. Acta* **2012**, *87*, 69–80. <https://doi.org/10.1016/j.gca.2012.03.028>.
- 541 (15) Muñoz, D.; Marcano, L.; Martín-Rodríguez, R.; Simonelli, L.; Serrano, A.; García-  
542 Prieto, A.; Fdez-Gubieda, M. L.; Muela, A. Magnetosomes Could Be Protective Shields  
543 against Metal Stress in Magnetotactic Bacteria. *Sci Rep* **2020**, *10* (1), 11430.  
544 <https://doi.org/10.1038/s41598-020-68183-z>.
- 545 (16) Blundy, J.; Wood, B. Partitioning of Trace Elements between Crystals and Melts.  
546 *Earth Planet. Sci. Lett.* **2003**, *210* (3–4), 383–397. [https://doi.org/10.1016/S0012-](https://doi.org/10.1016/S0012-821X(03)00129-8)  
547 [821X\(03\)00129-8](https://doi.org/10.1016/S0012-821X(03)00129-8).
- 548 (17) Burns, R. G. *Mineralogical Applications of Crystal Field Theory*; Cambridge  
549 University Press, 1993.
- 550 (18) McClure, D. S. The Distribution of Transition Metal Cations in Spinel. *Journal of*  
551 *Physics and Chemistry of Solids* **1957**, *3* (3), 311–317. [https://doi.org/10.1016/0022-](https://doi.org/10.1016/0022-3697(57)90034-3)  
552 [3697\(57\)90034-3](https://doi.org/10.1016/0022-3697(57)90034-3).
- 553 (19) Heyen, U.; Schuler, D. Growth and Magnetosome Formation by Microaerophilic  
554 Magnetospirillum Strains in an Oxygen-Controlled Fermentor. *Appl. Microbiol. Biotechnol.*  
555 **2003**, *61* (5–6), 536–544. <https://doi.org/10.1007/s00253-002-1219-x>.
- 556 (20) Tsvetkov, M.; Milanova, M.; Ivanova, I.; Neov, D.; Cherkezova-Zheleva, Z.;  
557 Zaharieva, J.; Abrashev, M. Phase Composition and Crystal Structure Determination of  
558 Cobalt Ferrite, Modified with Ce, Nd and Dy Ions by X-Ray and Neutron Diffraction. *Journal*  
559 *of Molecular Structure* **2019**, *1179*, 233–241. <https://doi.org/10.1016/j.molstruc.2018.07.083>.
- 560 (21) Amiri, S.; Shokrollahi, H. The Role of Cobalt Ferrite Magnetic Nanoparticles in  
561 Medical Science. *Materials Science and Engineering: C* **2013**, *33* (1), 1–8.  
562 <https://doi.org/10.1016/j.msec.2012.09.003>.
- 563 (22) Stokes, T. N.; Bromiley, G. D.; Gatta, G. D.; Rotiroti, N.; Potts, N. J.; Saunders, K.  
564 Cation Distribution and Valence in Synthetic Al–Mn–O and Fe–Mn–O Spinel under Varying  
565 Conditions. *Mineralogical Magazine* **2018**, *82* (4), 975–992.  
566 <https://doi.org/10.1180/mgm.2018.109>.
- 567 (23) Swatsitang, E.; Phokha, S.; Hunpratub, S.; Usher, B.; Bootchanont, A.; Maensiri, S.;  
568 Chindaprasirt, P. Characterization and Magnetic Properties of Cobalt Ferrite Nanoparticles.  
569 *Journal of Alloys and Compounds* **2016**, *664*, 792–797.  
570 <https://doi.org/10.1016/j.jallcom.2015.12.230>.
- 571 (24) Nakagomi, F.; da Silva, S. W.; Garg, V. K.; Oliveira, A. C.; Morais, P. C.; Franco  
572 Júnior, A.; Lima, E. C. D. The Influence of Cobalt Population on the Structural Properties of  
573 Co<sub>x</sub>Fe<sub>3-x</sub>O<sub>4</sub>. *Journal of Applied Physics* **2007**, *101* (9), 09M514.  
574 <https://doi.org/10.1063/1.2712821>.
- 575 (25) Staniland, S.; Williams, W.; Telling, N.; Van der Laan, G.; Harrison, A.; Ward, B.  
576 Controlled Cobalt Doping of Magnetosomes in Vivo. *Nat. Nanotechnol.* **2008**, *3* (3), 158–  
577 162. <https://doi.org/10.1038/nnano.2008.35>.
- 578 (26) Marcano, L.; Muñoz, D.; Martín-Rodríguez, R.; Orue, I.; Alonso, J.; García-Prieto, A.;  
579 Serrano, A.; Valencia, S.; Abrudan, R.; Fernández Barquín, L.; García-Arribas, A.; Muela,  
580 A.; Fdez-Gubieda, M. L. Magnetic Study of Co-Doped Magnetosome Chains. *J. Phys. Chem.*  
581 *C* **2018**, *122* (13), 7541–7550. <https://doi.org/10.1021/acs.jpcc.8b01187>.
- 582 (27) Chalmin, E.; Farges, F.; Brown, G. E. A Pre-Edge Analysis of Mn K-Edge XANES  
583 Spectra to Help Determine the Speciation of Manganese in Minerals and Glasses. *Contrib*

584 *Mineral Petrol* **2009**, *157* (1), 111–126. <https://doi.org/10.1007/s00410-008-0323-z>.

585 (28) Carta, D.; Casula, M. F.; Floris, P.; Falqui, A.; Mountjoy, G.; Boni, A.; Sangregorio,  
586 C.; Corrias, A. Synthesis and Microstructure of Manganese Ferrite Colloidal Nanocrystals.  
587 *Phys. Chem. Chem. Phys.* **2010**, *12* (19), 5074–5083. <https://doi.org/10.1039/B922646J>.

588 (29) Toksha, B. G.; Shirsath, S. E.; Mane, M. L.; Patange, S. M.; Jadhav, S. S.; Jadhav, K.  
589 M. Autocombustion High-Temperature Synthesis, Structural, and Magnetic Properties of  
590  $\text{CoCr}_x\text{Fe}_{2-x}\text{O}_4$  ( $0 \leq x \leq 1.0$ ). *J. Phys. Chem. C* **2011**, *115* (43), 20905–20912.  
591 <https://doi.org/10.1021/jp205572m>.

592 (30) Giri, A. K.; Kirkpatrick, E. M.; Moongkhamklang, P.; Majetich, S. A.; Harris, V. G.  
593 Photomagnetism and Structure in Cobalt Ferrite Nanoparticles. *Appl. Phys. Lett.* **2002**, *80*  
594 (13), 2341–2343. <https://doi.org/10.1063/1.1464661>.

595 (31) Hsueh, Y.-H.; Lin, K.-S.; Ke, W.-J.; Hsieh, C.-T.; Chiang, C.-L.; Tzou, D.-Y.; Liu, S.-  
596 T. The Antimicrobial Properties of Silver Nanoparticles in *Bacillus Subtilis* Are Mediated by  
597 Released  $\text{Ag}^+$  Ions. *PLOS ONE* **2015**, *10* (12), e0144306.  
598 <https://doi.org/10.1371/journal.pone.0144306>.

599 (32) Komeili, A. Molecular Mechanisms of Compartmentalization and Biomineralization  
600 in Magnetotactic Bacteria. *Fems Microbiol. Rev.* **2012**, *36* (1), 232–255.  
601 <https://doi.org/10.1111/j.1574-6976.2011.00315.x>.

602 (33) Brown, S. D.; Martin, M.; Deshpande, S.; Seal, S.; Huang, K.; Alm, E.; Yang, Y.; Wu,  
603 L.; Yan, T.; Liu, X.; Arkin, A.; Chourey, K.; Zhou, J.; Thompson, D. K. Cellular Response of  
604 *Shewanella Oneidensis* to Strontium Stress. *Applied and Environmental Microbiology* **2006**,  
605 *72* (1), 890–900. <https://doi.org/10.1128/AEM.72.1.890-900.2006>.

606 (34) Corradino, R. A.; Ebel, J. G.; Craig, P. H.; Taylor, A. N.; Wasserman, R. H. Calcium  
607 Absorption and the Vitamin D3-Dependent Calcium-Binding Protein. *Calc. Tis Res.* **1971**, *7*  
608 (1), 81–92. <https://doi.org/10.1007/BF02062596>.

609 (35) Alphantery, E.; Carvallo, C.; Menguy, N.; Chebbi, I. Chains of Cobalt Doped  
610 Magnetosomes Extracted from AMB-1 Magnetotactic Bacteria for Application in Alternative  
611 Magnetic Field Cancer Therapy. *J. Phys. Chem. C* **2011**, *115* (24), 11920–11924.  
612 <https://doi.org/10.1021/jp201274g>.

613 (36) Fazli, A.; Khataee, A.; Brigante, M.; Mailhot, G. Cubic Cobalt and Zinc Co-Doped  
614 Magnetite Nanoparticles for Persulfate and Hydrogen Peroxide Activation towards the  
615 Effective Photodegradation of Sulfalene. *Chem. Eng. J.* **2021**, *404*, 126391.  
616 <https://doi.org/10.1016/j.cej.2020.126391>.

617 (37) Huber, F.; Schild, D.; Vitova, T.; Rothe, J.; Kirsch, R.; Schaefer, T. U(VI) Removal  
618 Kinetics in Presence of Synthetic Magnetite Nanoparticles. *Geochim. Cosmochim. Acta* **2012**,  
619 *96*, 154–173. <https://doi.org/10.1016/j.gca.2012.07.019>.

620 (38) Crean, D. E.; Coker, V. S.; van der Laan, G.; Lloyd, J. R. Engineering Biogenic  
621 Magnetite for Sustained Cr(VI) Remediation in Flow-through Systems. *Environ. Sci. Technol.*  
622 **2012**, *46* (6), 3352–3359. <https://doi.org/10.1021/es2037146>.

623 (39) Baumgartner, J.; Carillo, M. A.; Eckes, K. M.; Werner, P.; Faivre, D. Biomimetic  
624 Magnetite Formation: From Biocombinatorial Approaches to Mineralization Effects.  
625 *Langmuir* **2014**, *30* (8), 2129–2136. <https://doi.org/10.1021/la404290c>.

626 (40) Eguchi, Y.; Fukumori, Y.; Taoka, A. Measuring Magnetosomal PH of the  
627 Magnetotactic Bacterium *Magnetospirillum Magneticum* AMB-1 Using PH-Sensitive  
628 Fluorescent Proteins. *Biosci. Biotechnol. Biochem.* **2018**, *82* (7), 1243–1251.  
629 <https://doi.org/10.1080/09168451.2018.1451739>.

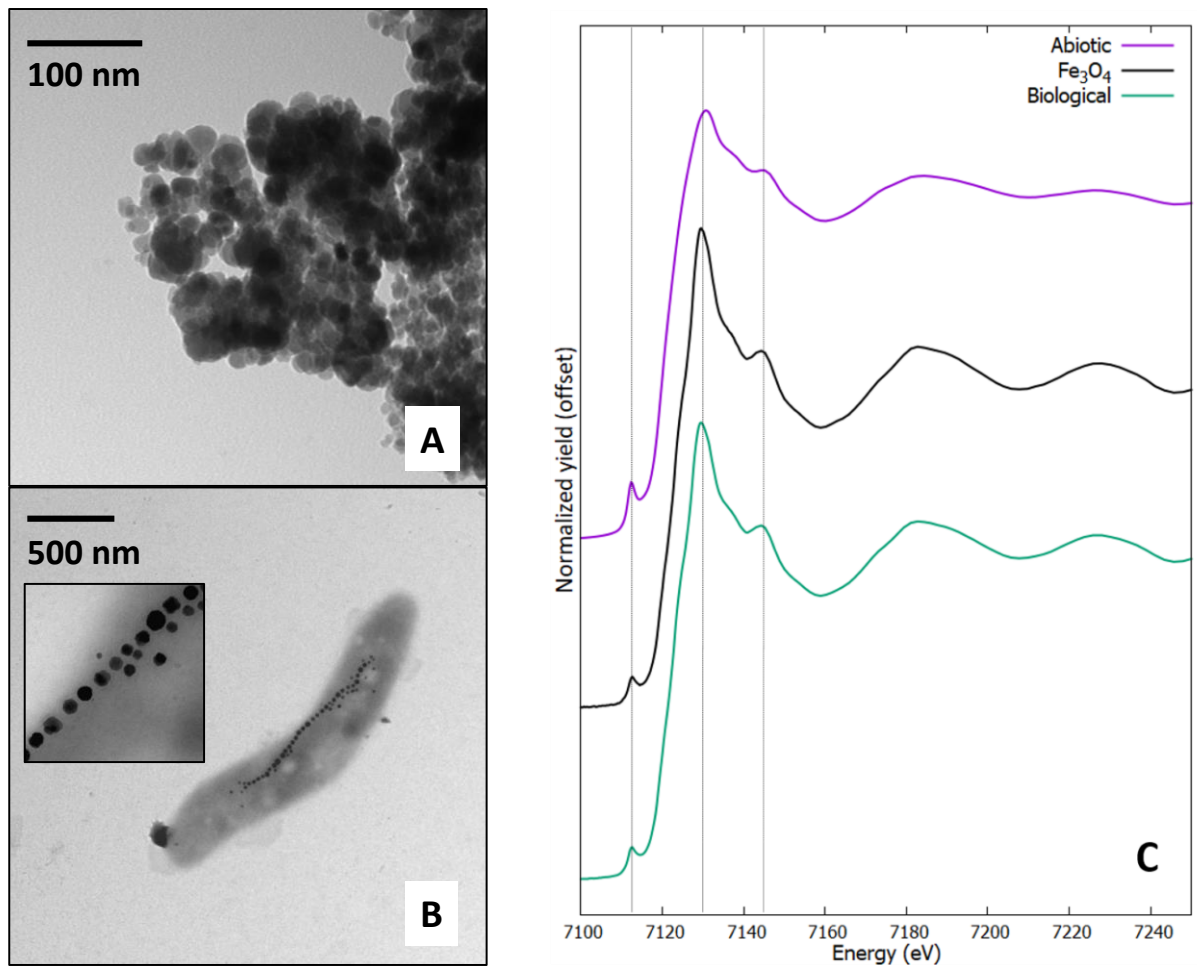
630 (41) Van der Lee, J.; De Windt, L. CHESS Tutorial and Cookbook. Updated for Version  
631 3.0, Manual Nr. LHM/RD/02/13.; Paris, 2002; p 116.

632 (42) Blanc, P.; Lassin, A.; Piantone, P.; Azaroual, M.; Jacquemet, M.; Fabbri, A.; Gaucher,  
633 E. C. Thermoddem: A Geochemical Database Focused on Low Temperature Water/Rock

634 Interactions and Waste Materials. *Appl. Geochem.* **2012**, 27 (10), 2107–2116.  
635 <https://doi.org/10.1016/j.apgeochem.2012.06.002>.  
636 (43) Chicot, D.; Mendoza, J.; Zaoui, A.; Louis, G.; Lepingle, V.; Roudet, F.; Lesage, J.  
637 Mechanical Properties of Magnetite (Fe<sub>3</sub>O<sub>4</sub>), Hematite (Alpha-Fe<sub>2</sub>O<sub>3</sub>) and Goethite (Alpha-  
638 FeO Center Dot OH) by Instrumented Indentation and Molecular Dynamics Analysis. *Mater.*  
639 *Chem. Phys.* **2011**, 129 (3), 862–870. <https://doi.org/10.1016/j.matchemphys.2011.05.056>.  
640 (44) Fine, M. E.; Kenney, N. T. Moduli and Internal Friction of Magnetite as Affected by  
641 the Low-Temperature Transformation. *Phys. Rev.* **1954**, 94 (6), 1573–1576.  
642 <https://doi.org/10.1103/PhysRev.94.1573>.  
643 (45) Gholizadeh, A. A Comparative Study of Physical Properties in Fe<sub>3</sub>O<sub>4</sub> Nanoparticles  
644 Prepared by Coprecipitation and Citrate Methods. *J. Am. Ceram. Soc.* **2017**, 100 (8), 3577–  
645 3588. <https://doi.org/10.1111/jace.14896>.  
646 (46) Blundy, J.; Wood, B. Prediction of Crystal-Melt Partition-Coefficients from Elastic-  
647 Moduli. *Nature* **1994**, 372 (6505), 452–454. <https://doi.org/10.1038/372452a0>.  
648 (47) van Hinsberg, V. J.; Migdisov, A. A.; Williams-Jones, A. E. Reading the Mineral  
649 Record of Fluid Composition from Element Partitioning. *Geology* **2010**, 38 (9), 847–850.  
650 <https://doi.org/10.1130/G31112.1>.  
651 (48) Pimenov, A.; Tachos, S.; Rudolf, T.; Loidl, A.; Schrupp, D.; Sing, M.; Claessen, R.;  
652 Brabers, V. A. M. Terahertz Conductivity at the Verwey Transition in Magnetite. *Phys. Rev.*  
653 *B* **2005**, 72 (3), 035131. <https://doi.org/10.1103/PhysRevB.72.035131>.  
654 (49) Zulfiqar; Afzal, S.; Khan, R.; Zeb, T.; Rahman, M. ur; Burhanullah; Ali, S.; Khan, G.;  
655 Rahman, Z. ur; Hussain, A. Structural, Optical, Dielectric and Magnetic Properties of PVP  
656 Coated Magnetite (Fe<sub>3</sub>O<sub>4</sub>) Nanoparticles. *J Mater Sci: Mater Electron* **2018**, 29 (23), 20040–  
657 20050. <https://doi.org/10.1007/s10854-018-0134-6>.  
658 (50) Shannon, R. D.; Prewitt, C. T. Effective Ionic Radii in Oxides and Fluorides. *Acta*  
659 *Crystallographica Section B* **1969**, 25 (5), 925–946.  
660 <https://doi.org/10.1107/S0567740869003220>.  
661

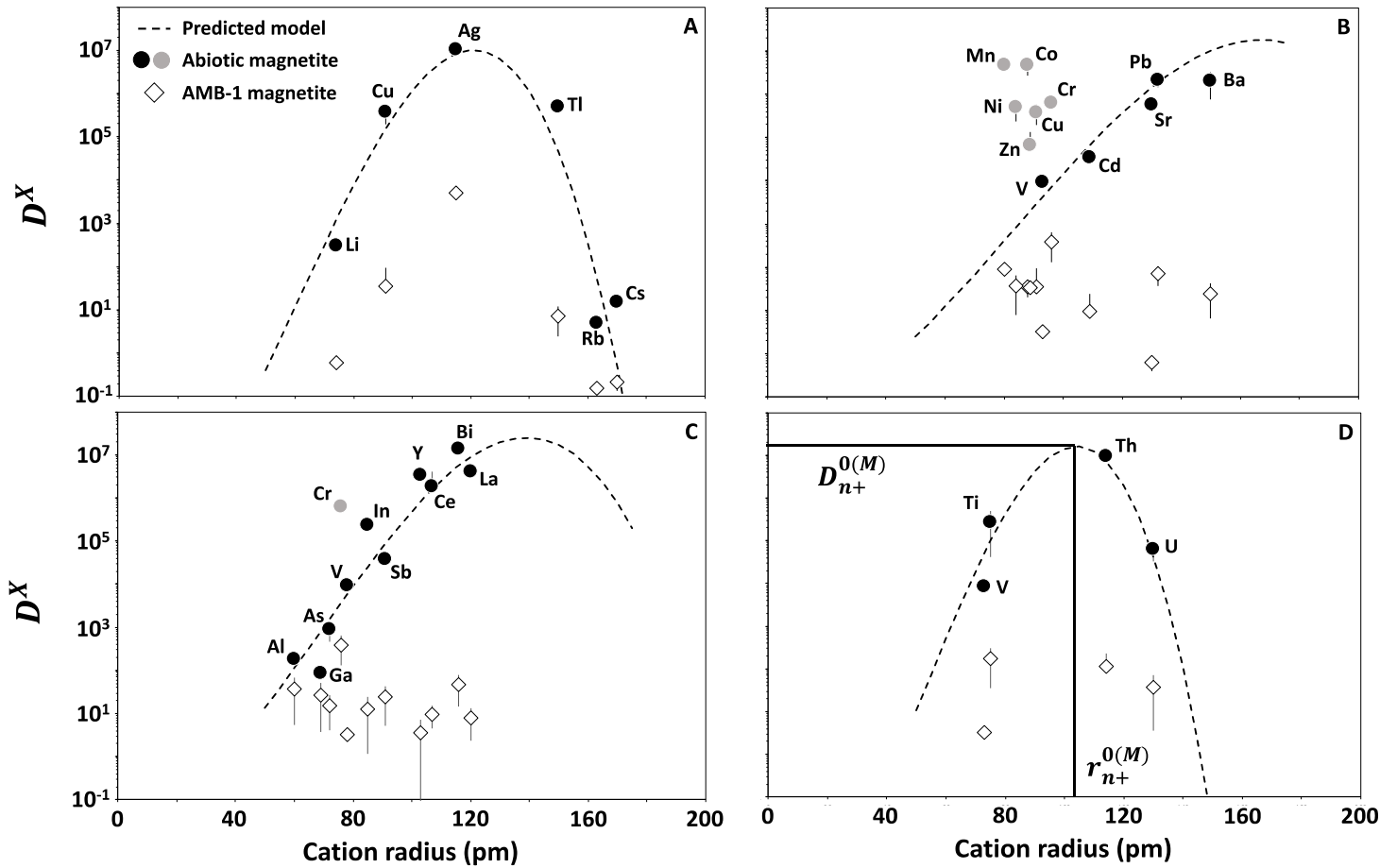
662

663 **Figures**



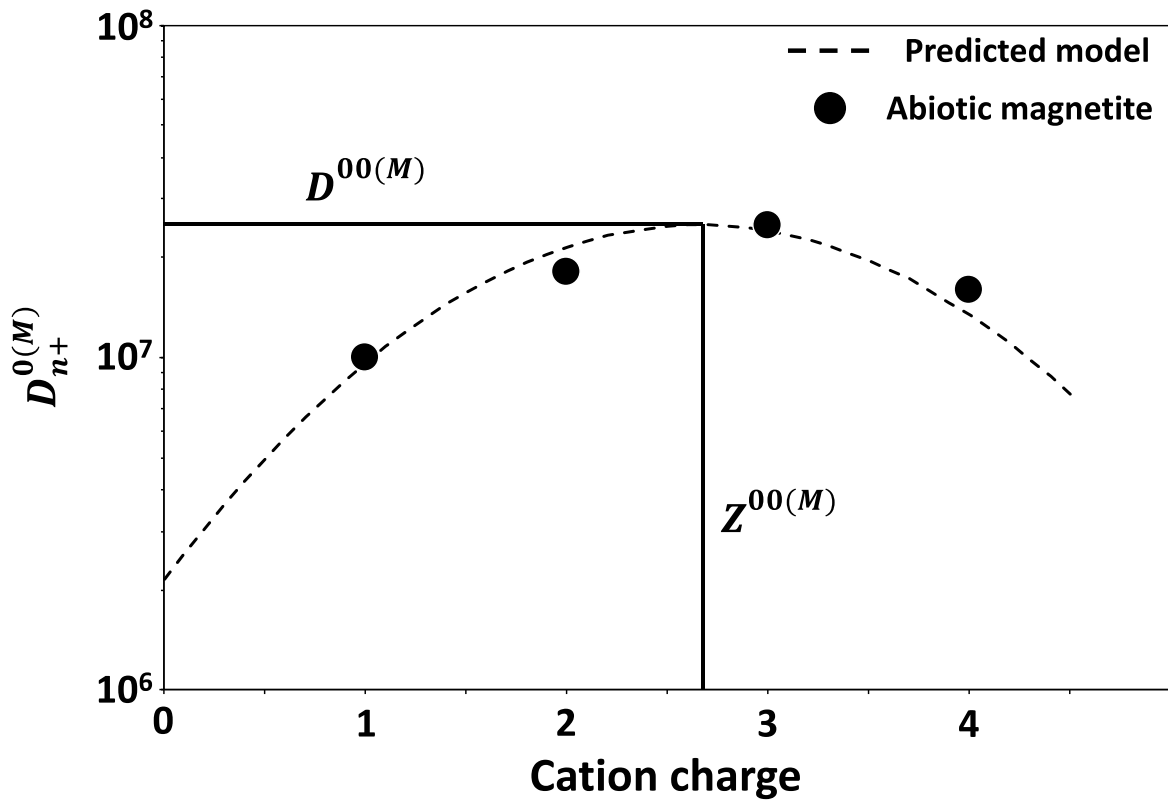
664  
665  
666  
667  
668  
669

**Figure 1.** Transmission electron microscopy images of (A) abiotic magnetite nanoparticles and (B) MSR-1 bacteria containing magnetite nanoparticles in magnetosomes (inset, magnified region of magnetosome chain). (C) Fe K-edge X-ray absorption near-edge structure spectra of abiotic and biological magnetite nanoparticles with magnetite reference.



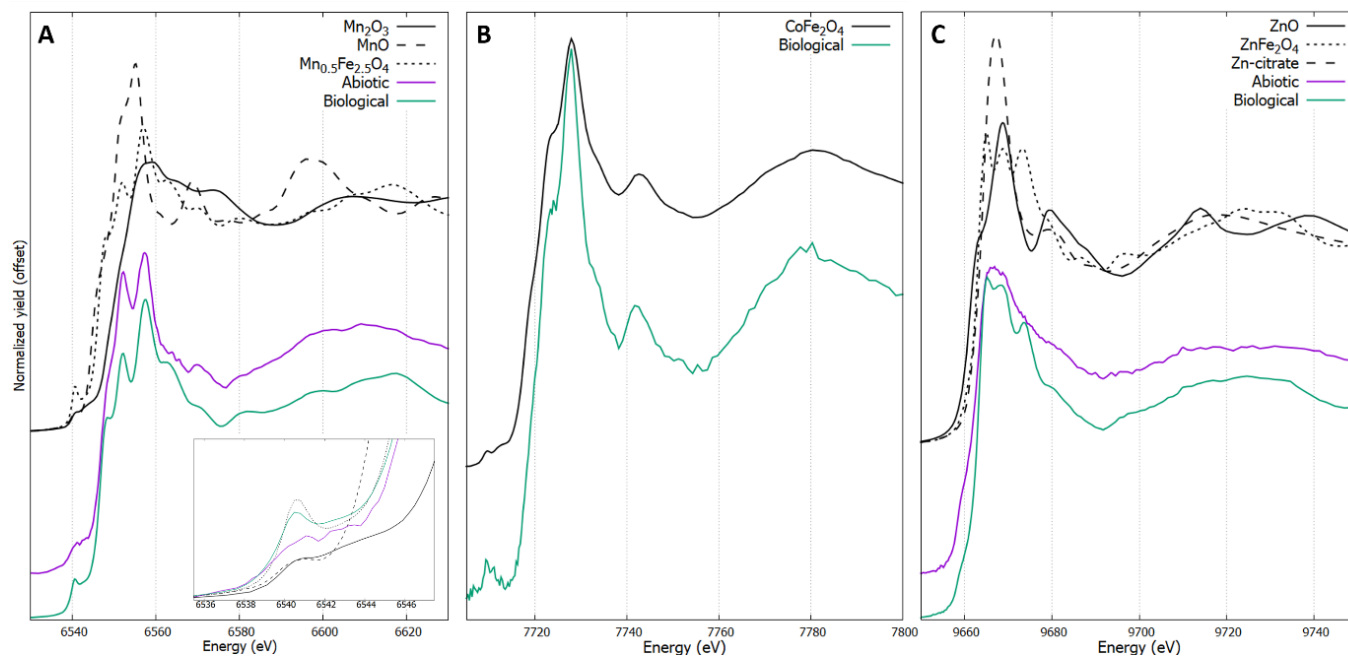
670  
 671  
 672  
 673  
 674  
 675  
 676  
 677  
 678  
 679  
 680

**Figure 2.** Partition coefficients ( $D^X$ ) of (A) monovalent, (B) divalent, (C) trivalent and (D) tetravalent cations in the case of abiotic (black and grey circles) and biological (AMB-1, open diamonds) magnetite. Dashed line indicate the predicted values of  $D^X$  based on a lattice strain model (Eq. 2). Grey symbols point to 3d metals [Co(II), Cr(II), Cr(III), Cu(II), Mn(II), Ni(II), Zn(II)] showing variations from the predicted values in the abiotic precipitation of magnetite. Cation radius taken from Shannon and Prewitt and summarized in Table S7<sup>50</sup>. Black lines in (D) indicate the position of ideal cation radius ( $r_{n+}^{0(M)}$ ) and strain-compensated partition coefficient ( $D_{n+}^{0(M)}$ ).



681  
 682  
 683  
 684  
 685  
 686  
 687  
 688  
 689

**Figure 3.** Strain-compensated partition coefficients ( $D_{n+}^{0(M)}$ ) for each element valence extracted from Figs. 2A to 2D. The predicted model was calculated using Eq. 3 and considering published values of magnetite’s dielectric constant of 50 and a lattice region with a radius of 17 nm corresponding to the size of magnetite nanoparticles (see Materials and Methods for details). Black lines indicate the position of ideal charge ( $Z^{00(M)}$ ) and strain-compensated partition coefficient causing no electrostatic charging ( $D^{00(M)}$ ).

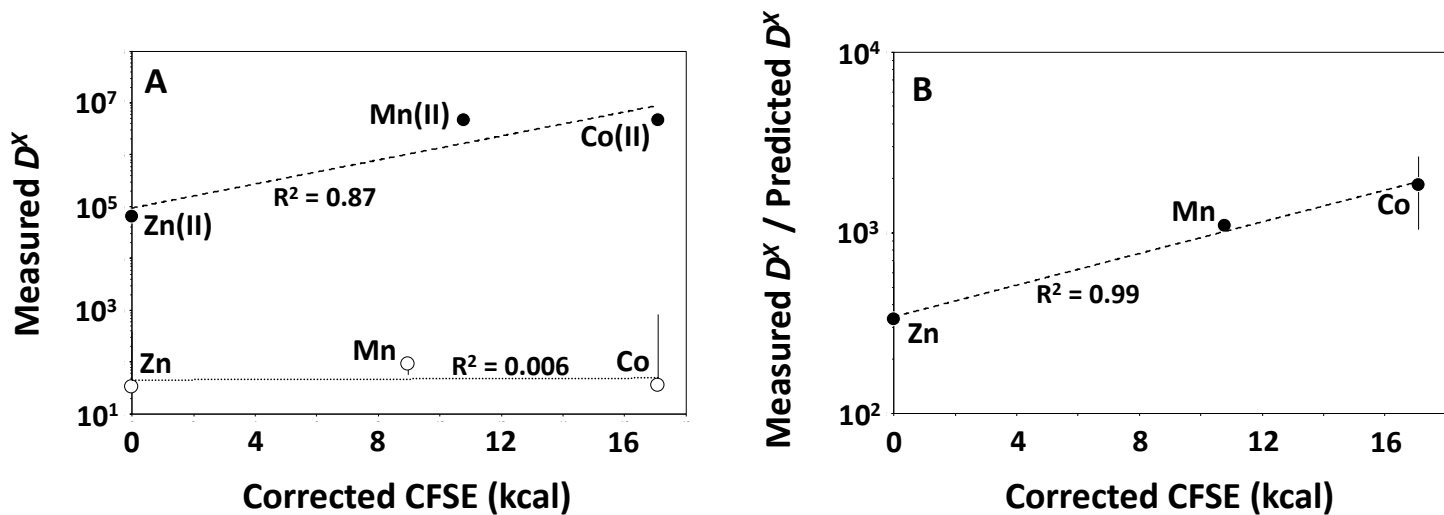


690

691

692 **Figure 4.** X-ray absorption near edge structure (XANES) of doped abiotic and biological  
 693 magnetite nanoparticles with reference materials at (A) Mn K-edge (inset, pre-edge region), (B)  
 694 Co K-edge and (C) Zn K-edge.

695

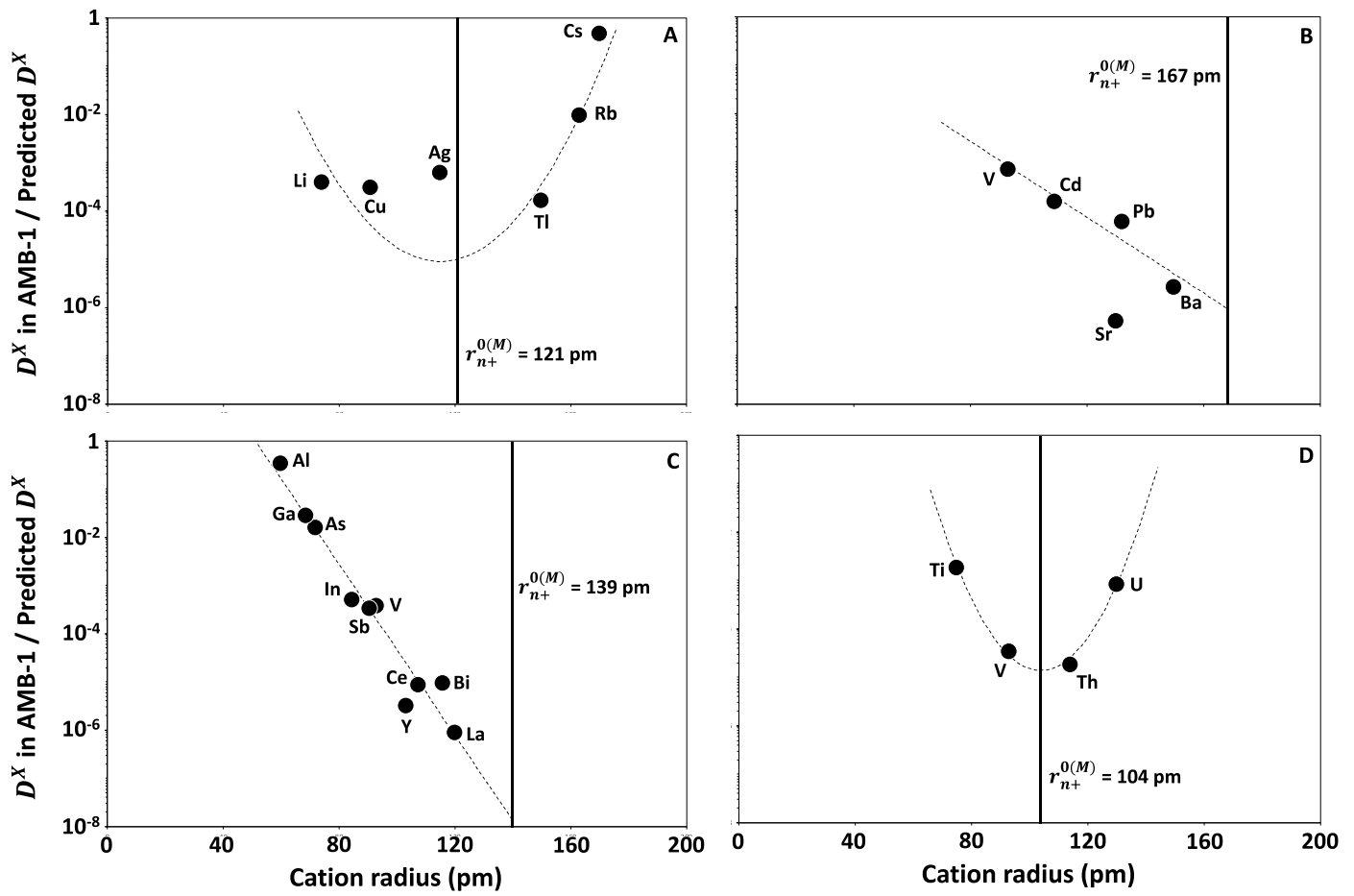


696

697

698 **Figure 5.** (A) Partition coefficients ( $D^X$ ) and (B) ratio of measured partition coefficients and  
 699 partition coefficients predicted from a lattice strain theory (Eq. 2) of Mn, Co and Zn represented  
 700 against their XAS-corrected Crystal Field Stabilization Energy (CFSE). Black and open  
 701 symbols represent abiotic and biological conditions, respectively.

702



703  
 704  
 705  
 706  
 707  
 708  
 709  
 710  
 711

**Figure 6.** Biological  $D^X$  obtained from AMB-1 cultures normalized to the  $D^X$  predicted from lattice strain theory (Eq. 2) in the case of (A) monovalent, (B) divalent, (C) trivalent and (D) tetravalent elements.  $r_{n+}^{0(M)}$  values reported here are extracted from Fig. 2 and Table S3.